

Spin thermometry and spin relaxation of optically detected Cr³⁺ ions in ruby Al₂O₃Vikas K. Sewani^{1,*}, Rainer J. Stöhr², Roman Kolesov², Hyma H. Vallabhapurapu¹,
Tobias Simmet³, Andrea Morello¹ and Arne Laucht^{1,†}¹Centre for Quantum Computation and Communication Technology, School of Electrical Engineering and Telecommunications,
UNSW Sydney, Sydney, New South Wales 2052, Australia²3rd Physikalisches Institut, Universität Stuttgart, 70569 Stuttgart, Germany³Walter Schottky Institut and Physik Department, Technische Universität München, 85748 Garching, Germany

(Received 16 July 2020; accepted 8 September 2020; published 25 September 2020)

Paramagnetic ions in solid state crystals form the basis for many advanced technologies such as lasers, masers, frequency standards, and quantum-enhanced sensors. One of the most-studied examples is the Cr³⁺ ion in sapphire (Al₂O₃), also known as ruby, which has been intensely studied in the 1950s and 1960s. However, despite decades of research on ruby, some of its fundamental optical and spin properties have not yet been characterized at ultralow temperatures. In this paper, we present optical measurements on a ruby crystal in a dilution refrigerator at ultralow temperatures down to 20 mK. Analyzing the relative populations of its ⁴A₂ ground-state spin levels, we extract a lattice temperature of 143 ± 7 mK under continuous laser excitation. We perform spin-lattice relaxation T₁ measurements in excellent agreement with the direct, one-phonon model. Furthermore, we perform optically detected magnetic resonance measurements showing magnetically driven transitions between the ground-state spin levels for various magnetic fields. Our measurements characterize some of ruby's low-temperature spin properties, and lay the foundations for more advanced spin control experiments.

DOI: [10.1103/PhysRevB.102.104114](https://doi.org/10.1103/PhysRevB.102.104114)**I. INTRODUCTION**

In addition to being a popular gemstone, ruby (Cr³⁺ in Al₂O₃) has also been investigated for its optical and spin properties for over 150 years [1,2], and has played an important role in the history of lasers [3] and masers [4]. However, despite decades of research, it has rarely been measured at temperatures $T < 1$ K [5–8], and fundamental properties, such as its electron spin relaxation, need to be investigated. In particular, the spin relaxation of the 3d³ orbital ground state of Cr³⁺, which consists of an $S = 3/2$ Kramer's doublet with a zero-field splitting of ~11.49 GHz (corresponding to the thermal energy at $T = 550$ mK), has only been measured at temperatures as low as $T = 1.6$ K, where a maximum relaxation time of $T_1 = 560$ ms was measured [9]. For ruby crystals with sufficiently low Cr³⁺ concentrations (<0.01%), the spin relaxation follows a $T_1(T) \propto T^{-1}$ relationship down to this temperature, corresponding to a one-phonon (direct) process [9,10]. Assuming the one-phonon model continues to dominate at lower temperatures, a saturation of the T_1 can only be expected below $T = 550$ mK at zero external magnetic field.

In this paper, we perform optical measurements on a ruby crystal inside a dilution refrigerator with base temperature $T_{\text{MXC}} = 20$ mK. By mapping out the population ratio of the Zeeman-split $|\pm 3/2\rangle_g$ spin states as a function of magnetic field, we conduct optical thermometry of the ruby lattice

temperature, and measure $T_{\text{Ruby}} = 143 \pm 7$ mK under 15 nW resonant laser excitation. This proves that a very low temperature of the ruby sample can be maintained under sufficiently low continuous laser excitation. We then measure the spin T_1 decay of the Cr³⁺ ground state using an all-optical method at ultralow temperatures. We obtain a maximum $T_1 = 3.67 \pm 0.35$ s, and observe that the spin relaxation can be completely described by a direct, one-phonon process.

Furthermore, we demonstrate optically detected magnetic resonance (ODMR) of the Cr³⁺ ground state. Previously, electron paramagnetic resonance (EPR) spectroscopy has been utilized to probe the Zeeman level splitting of the ⁴A₂ ground state in an EPR spectrometer [11–13], and more recently via coupling to a microwave whispering gallery mode [5,6,14], or a coplanar waveguide [7,8]. Optically detected readout has been shown to provide access to both the spin population of the optically excited $\bar{E}(^2E)$ state [15,16], as well as of the ⁴A₂ ground state through broadband optical pumping via spin memory when the external magnetic field is aligned with the c axis of the crystal [15,17]. In our experiment, we use resonant laser excitation for spin initialization and readout [18], which improves our spatial resolution to ~1 μm² and strongly reduces the number of ions that are probed compared to EPR spectroscopy. Additionally, it allows the magnetic field to be applied nonparallel to the c axis of the crystal, providing access to clock transitions [12], where the coherence times of the spins are expected to be much longer. A printed circuit board (PCB) antenna, mounted in the vicinity of the sample, allows us to magnetically drive the ground-state electron spins. While not demonstrated in this paper, the combination of resonant laser readout with a PCB or on-chip microwave

*v.sewani@student.unsw.edu.au

†a.laucht@unsw.edu.au

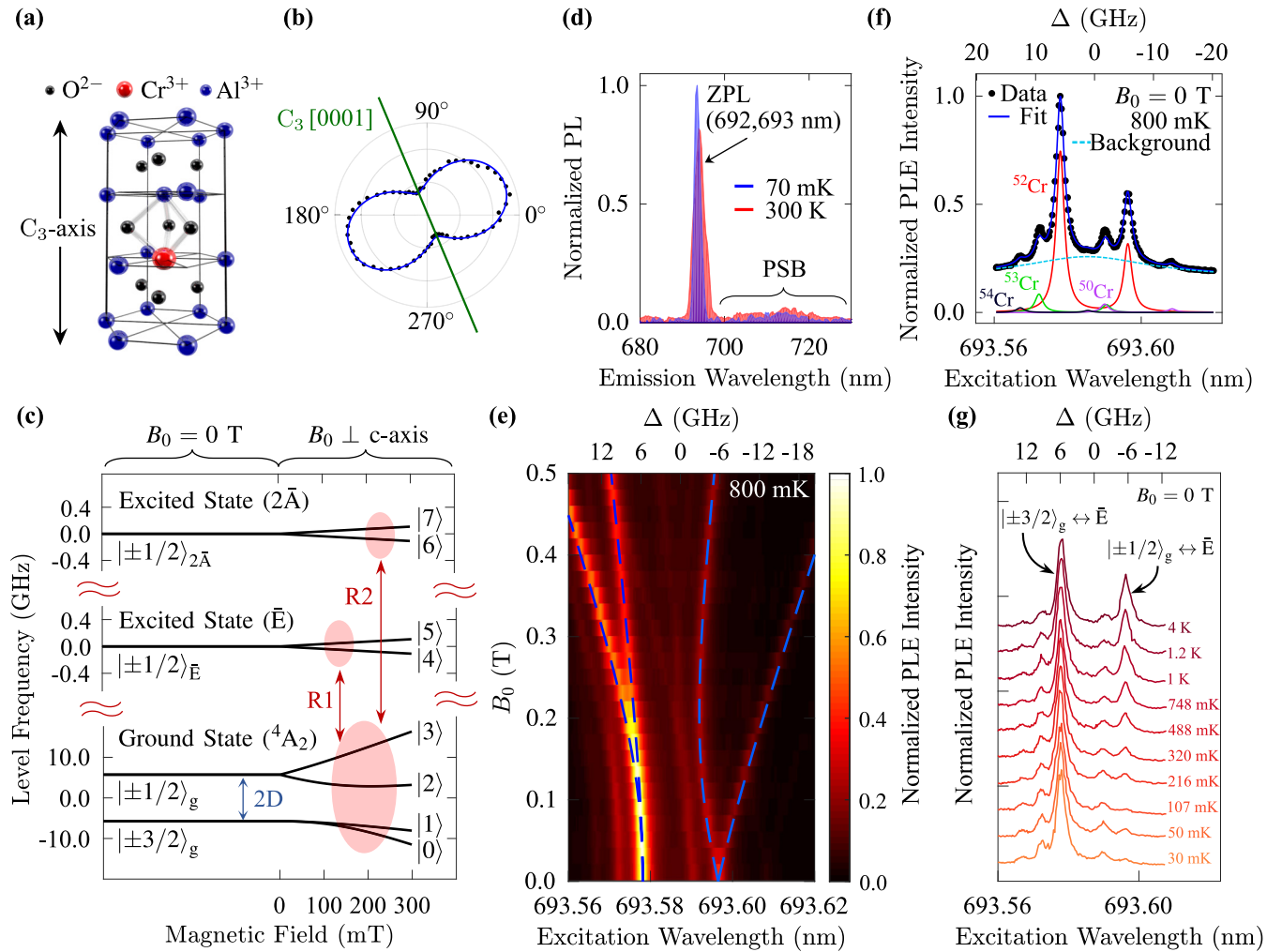


FIG. 1. (a) Hexagonal crystal structure of Al_2O_3 containing a single interstitial Cr^{3+} ion. (b) Polarization dependence of the phonon sideband (PSB) emission with excitation laser in resonance with the $|\pm 3/2\rangle_g \leftrightarrow \bar{E}$ transition at $B_0 = 0$ T. (c) Electronic level scheme of Cr^{3+} in Al_2O_3 at $B_0 = 0$ T and $B_0 \perp c$ axis. (d) Emission spectrum of ruby with 520 nm (off-resonant) excitation at room temperature (red curve) and $T_{\text{MXC}} = 70$ mK (blue curve). Marked are the zero-phonon lines (ZPLs) used for resonant excitation and the PSB used for signal detection in all further experiments. (e) PLE spectrum as a function of magnetic field for $B_0 \perp c$ axis. The overlaid, dashed blue lines correspond to the Hamiltonian in Eq. (1) with parameters $g = 1.982$, $-2D = 11.460$ GHz, and 693.587 nm as the splitting between the midpoint of $|\pm 1/2\rangle_g$ and $|\pm 3/2\rangle_g$, and \bar{E} . The quantity Δ (top x axis) denotes the detuning in laser excitation energy (in frequency units) from the midpoint of the ^{52}Cr $|\pm 1/2\rangle_g \leftrightarrow \bar{E}$ and $|\pm 3/2\rangle_g \leftrightarrow \bar{E}$ transitions. (f) Zero-field photoluminescence excitation (PLE) spectrum showing multiple peaks that are associated with the different Cr isotopes. Peaks are fitted with Lorentzian functions with their relative peak intensities fixed to correspond to the isotopes' natural abundance (4.3% for ^{50}Cr , 83.8% for ^{52}Cr , 9.5% for ^{53}Cr , and 2.4% for ^{54}Cr [21]). (g) PLE spectrum at $B_0 = 0$ T for varying mixing chamber (MXC) temperatures, where the temperature readings are given by the MXC thermometer. Increased PLE intensity from the $|\pm 1/2\rangle_g \leftrightarrow \bar{E}$ transition is in accordance with the redistribution of spin population at increased temperature.

(MW) antenna not only allows spectroscopic but also coherence time investigations. This adds to the spin characterization tools available for the future study of the Cr^{3+} defect in ruby.

II. SPIN HAMILTONIAN

In ruby, some of the Al^{3+} ions (usually much less than 1%) of the Al_2O_3 crystal are replaced by Cr^{3+} ions with three unpaired electrons in their outer $3d^3$ shell. Each Cr^{3+} ion is surrounded by six O^{2-} ions in the form of a distorted octahedron [see Fig. 1(a)] [2]. The electrostatic crystal field, which the chromium ions are subject to, lift the $3d$ orbital degeneracy

of the 4A_2 , \bar{E} , and $2\bar{A}$ levels, as shown in the energy level diagram in Fig. 1(c). In the ground state (4A_2), the chromium ions are additionally subject to a trigonal crystal field, and together with spin-orbit coupling, the spin degeneracy is lifted, leaving a Kramers doublet with the degenerate pairs $|\pm 1/2\rangle$ and $|\pm 3/2\rangle$, with the latter being the spin ground state [19,20]. At cryogenic temperatures, the higher excited orbital states \bar{E} and $2\bar{A}$ are 1.7876 eV (693.6 nm) and 1.792 eV (692.2 nm) above 4A_2 . Due to their emission in the red part of the spectrum, they are referred to as the R_1 and R_2 lines, respectively [2]. Equation (1) shows the effective system Hamiltonian of the 4A_2 ground state (\mathcal{H}_0), and Eq. (2) shows the Hamiltonian of

the \bar{E} ($\mathcal{H}_{\bar{E}}$) and $2\bar{A}$ ($\mathcal{H}_{2\bar{A}}$) excited states, which are the same up to their g -factors,

$$\mathcal{H}_0 = g_{\parallel}\mu_B B_z S_z + g_{\perp}\mu_B (B_x S_x + B_y S_y) + D[S_z^2 - \frac{1}{3}S(S+1)], \quad (1)$$

$$\mathcal{H}_{\bar{E},2\bar{A}} = g_{\parallel}\mu_B B_z S_z + g_{\perp}\mu_B (B_x S_x + B_y S_y). \quad (2)$$

The z axis for \mathcal{H}_0 and $\mathcal{H}_{\bar{E},2\bar{A}}$ is defined along the Al_2O_3 crystal axis (c axis) direction, while the x axis and y axis are arbitrarily oriented. For \mathcal{H}_0 (4A_2), $S = 3/2$ where $S_{x,y,z}$ are the corresponding spin matrices, $B_{x,y,z}$ are the vector components of an externally applied magnetic field, μ_B is the Bohr's magneton, $-2D = 11.493 \pm 0.004$ GHz is the zero-field splitting, and $g_{\parallel} = 1.9817 \pm 0.0004$ and $g_{\perp} = 1.9819 \pm 0.0006$ are the room-temperature g -factors parallel and perpendicular to the c axis [22]. The Hamiltonians $\mathcal{H}_{\bar{E}}$ and $\mathcal{H}_{2\bar{A}}$ for the excited states consist of only Zeeman terms, where $S_{x,y,z}$ are the $S = 1/2$ spin matrices, $g_{\parallel} = -2.445$ and $g_{\perp} = 0.0515$ for \bar{E} [23], and $g_{\parallel} = 1.46$ and $g_{\perp} \approx 0$ for $2\bar{A}$ [24,25].

In our experiments, we fix $B_0 \perp C_3[0001]$ axis. Additionally, our optics axis is parallel to B_0 , which allows us to determine the orientation of the $C_3[0001]$ axis with respect to our optical setup with a laser polarization dependence measurement, as shown in Fig. 1(b) [19,26]. The energy levels as a function of magnetic field for $B_0 \perp c$ axis are shown in Fig. 1(c). For finite values of B_0 , \mathcal{H}_0 contains off-diagonal terms and hence does not commute with the S_z spin matrix. This results in the eigenstates consisting of superpositions of the pure spin $S = 3/2$ eigenstates with their quantization along the C_3 symmetry axis. We hence label all states canonically from $|0\rangle$ to $|7\rangle$ as shown. See also Ref. [12] for a detailed study of the magnetic field direction dependence of the eigenvalues and eigenstates of \mathcal{H}_0 .

III. EXPERIMENTAL SETUP

We perform our measurements on a monocrystalline ruby sample with a Cr^{3+} concentration of 0.005%. For optical excitation, we either use a 520-nm laser diode for off-resonant excitation, or a continuous-wave Ti:sapphire laser, tunable between 692 and 1000 nm with an optical linewidth < 50 kHz and referenced with a wave meter, for resonant excitation of the R_1 line. In either case, the collimated beam enters the dilution refrigerator from the top through a vacuum-sealed, antireflective window, and propagates down the cryostat through small apertures ($D = 7$ mm) in the baffles of the 50, 4, and 1 K plates. The laser beam is incident on an objective lens [Olympus MS Plan 50 \times /0.80 numerical aperture (NA)], which is mounted to the cold finger attached to the mixing chamber (MXC) plate. The laser beam then gets focused through a 1-mm hole in a printed circuit board (PCB) that carries the MW antenna [27], which delivers the oscillating magnetic field $B_1 \parallel B_0$ for the ODMR experiments in Sec. VII. The laser is focused onto the ruby sample, which is mounted on top of a three-axis *Attocube* stage on the same cold finger, and thermalized through an *Attocube* thermal coupling link. The ruby sample is positioned in the homogeneous region at the center of a superconducting electromagnet, which delivers

the static magnetic field B_0 . The sample's c axis is perpendicular to the B_0 direction ($B_0 \perp c$ axis).

The photoluminescence (PL) from an ensemble of Cr^{3+} ions is collimated by the same objective lens, and travels through the same path as discussed before, for detection outside the fridge. The PL signal is coupled into a 50- μm multimode fiber, and detection is performed with either a minispectrometer or a single-photon avalanche diode (SPAD). The PL spectrum obtained with off-resonant excitation is shown in Fig. 1(d) at room temperature (red line) and $T_{\text{MXC}} = 70$ mK (blue curve). The zero-phonon line (ZPL) is clearly visible in both cases, resulting from PL from both the R_1 and R_2 lines. Additionally, a wide phonon sideband (PSB) is visible on the low-energy side of the ZPL. For all further measurements, we resonantly excite the R_1 line, and detect the PL from the PSB by placing a 700-nm long-pass and a 800-nm short-pass filter into the detection path.

In order to generate the control sequences and synchronize the different pieces of equipment, we use a transistor-transistor logic (TTL) pulse generator (*PulseBlasterESR-PRO 250*). The output of the Ti:sapphire laser is amplitude modulated by the TTL pulses through an acousto-optic modulator. The MW drive, delivered by the PCB antenna, is modulated via the built-in pulse modulation of the MW source. Finally, the digitizer used to record the single-photon detection events from the SPAD is gated, allowing us to temporally select when we would like the digitizer to store and count pulses with respect to the laser and MW pulses.

IV. PHOTOLUMINESCENCE EXCITATION SPECTROSCOPY

We start by employing photoluminescence excitation (PLE) spectroscopy to determine the R_1 optical absorption lines as a function of B_0 . When the Ti:sapphire laser is in resonance with an absorption line, the excitation rate from the respective ground-state level is increased, resulting in an increased PL from both the ZPL and PSB. At $B_0 = 0$ T, we only expect to see two optical transitions originating from $|\pm 1/2\rangle_g \leftrightarrow \bar{E}$ and $|\pm 3/2\rangle_g \leftrightarrow \bar{E}$, while at $B_0 > 0$, a total of four transitions can be observed within the R_1 line [see also Fig. 1(c)]. We plot the PLE spectra in Fig. 1(e) up to $B_0 = 0.5$ T. The measurement is performed at a temperature ($T_{\text{MXC}} = 800$ mK) $> (2D\hbar/k_B = 550$ mK) to allow for sufficient thermal population of the $|\pm 1/2\rangle_g$ state. Up to this magnetic field, we expect the Zeeman splitting of \bar{E} to be < 360 MHz owing to the small value of $g_{\perp} = 0.0515$ [see also Eq. (2)]. As this is much smaller than the optical linewidths of the PLE transitions (~ 1.8 GHz), the Zeeman splitting of \bar{E} cannot be observed, and the ground-state Hamiltonian \mathcal{H}_0 dominates the PLE spectra. The most prominent transitions in Fig. 1(e) are in good agreement with Eq. (1), and can be attributed to the R_1 transitions of the ${}^{52}\text{Cr}$ isotope, based on its natural abundance of 83.8%. Other isotopes of chromium result in a blueshift or redshift of the R_1 lines, and hence appear as dimmer copies near the dominant lines, as seen in Figs. 1(e) and 1(f). Of these isotopes, ${}^{53}\text{Cr}$ carries a nuclear spin of $I = 3/2$ which couples to the electron spin through a hyperfine interaction of $A = 48.5$ MHz [28].

In order to probe the effect of temperature on the relative strengths of the absorption lines, we vary the temperature of the dilution refrigerator and plot the measured PLE spectra at $B_0 = 0$ T in Fig. 1(g). The MXC temperature T_{MXC} is altered via a resistive heater mounted on the MXC plate, and is measured by the MXC thermometer. At lower temperatures, T_{MXC} is not a good measure of the lattice temperature near the Cr^{3+} ions under investigation. This is due to (i) the imperfect thermalization of the ruby sample to the MXC, (ii) local heating due to laser irradiation, and (iii) limited cooling power of the fridge. However, quenching of the $\pm|1/2\rangle_g \leftrightarrow \bar{E}$ transition and greater spin polarization in the $\pm|3/2\rangle_g$ state for $T_{\text{MXC}} < 500$ mK in Fig. 1(g) confirm that a lattice temperature < 550 mK is achieved. We will determine the exact lattice temperature by conducting optical thermometry on the Cr^{3+} ions in the next section (Sec. V).

V. OPTICAL THERMOMETRY

For the measurements shown in Fig. 1(g), we could only state the temperatures obtained from the MXC thermometer T_{MXC} , which most certainly differ from the actual lattice temperatures T_{Ruby} . While T_{Ruby} can be inferred from Cr^{3+} spin relaxation measurements for temperatures $T_{\text{MXC}} > 550$ mK (see Sec. VI), we can also extract T_{Ruby} from the relative spin populations of any two-level system in the ground state with splitting $\sim k_B T_{\text{Ruby}}$. For the measurements in this section (see Fig. 2), we choose the $|\pm 3/2\rangle_g$ states, that split into $|0\rangle$ and $|1\rangle$ subject to a magnetic field [see also Sec. II and Fig. 1(c)]. At $B_0 = 0.3$ T, the $|0\rangle$ and $|1\rangle$ states can be clearly resolved, and their level splitting is 3.46 GHz [from Eq. (1)] which corresponds to the thermal energy at $T = 166$ mK. We determine their relative populations by performing a PLE scan similar to Fig. 1(e), where the PL intensity is proportional to the spin population. A laser excitation power of 15 nW is used to avoid the effects of optical cycling, which would deviate the electron populations away from their thermal distributions (see Appendix C). This is in contrast to the T_1 measurements performed in Sec. VI, where a 1 μW laser excitation power is required to deviate the system sufficiently from thermal equilibrium, enabling us to measure the decay of the spin population over the relaxation duration.

The results of the optical thermometry method described above are shown in Fig. 2(a), where we plot the PLE spectra of the $|0\rangle \leftrightarrow \bar{E}$ and $|1\rangle \leftrightarrow \bar{E}$ transitions as a function of B_0 for $T_{\text{MXC}} = 20, 173,$ and 300 mK. In Fig. 2(b), we extract the PL intensity ratio of these two transitions—which is proportional to the population ratio of $|0\rangle$ and $|1\rangle$ —for $0.3 \leq B_0 \leq 0.42$ T, and fit this ratio to the Boltzmann distribution,

$$\frac{N_{|0\rangle}(B_0)}{N_{|1\rangle}(B_0)} = \exp\left(\frac{E_{|1\rangle}(B_0) - E_{|0\rangle}(B_0)}{k_B T_{\text{Ruby}}}\right), \quad (3)$$

where $E_{|0\rangle,|1\rangle}(B_0)$ are the energies of the states $|0\rangle, |1\rangle$ as a function of B_0 , obtained from Eq. (1). We find that at $T_{\text{MXC}} = 20$ mK the lattice temperature $T_{\text{Ruby}} = 143 \pm 7$ mK is significantly higher, due to local heating from the laser and insufficient thermalization of the sample. Nonetheless, this measurement verifies that lattice temperatures < 150 mK are achievable in optical experiments under continuous laser excitation, similar to what has been demonstrated

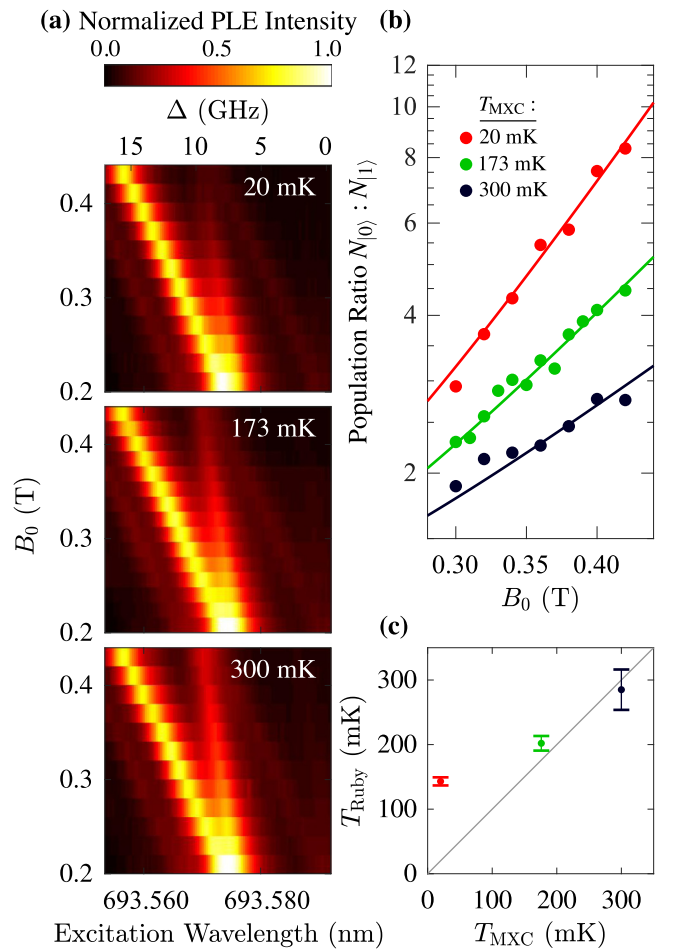


FIG. 2. (a) Normalized PLE spectra of the $|0\rangle \leftrightarrow \bar{E}$ and $|1\rangle \leftrightarrow \bar{E}$ transitions at $T_{\text{MXC}} = 20, 173,$ and 300 mK. (b) Ratio of PLE peak intensities (circles) extracted from (a) as a function of magnetic field. The solid lines are fits to the Boltzmann distribution, determining $T_{\text{Ruby}} = 143 \pm 7, 202 \pm 12,$ and 285 ± 31 mK for $T_{\text{MXC}} = 20, 173,$ and 300 mK, respectively. (c) Extracted T_{Ruby} vs T_{MXC} .

with self-assembled quantum dots in Ref. [29]. At $T_{\text{MXC}} = 173$ mK, we measure $T_{\text{Ruby}} = 202 \pm 12$ mK, and at $T_{\text{MXC}} = 300$ mK, we measure $T_{\text{Ruby}} = 285 \pm 31$ mK [data summarized in Fig. 2(c)]. These results show that, under these experimental conditions, the ruby sample is fully thermalized with the MXC at $T_{\text{MXC}} \approx 300$ mK.

VI. SPIN-LATTICE RELAXATION

We now measure the temperature dependence of the spin relaxation time T_1 from the $\pm|1/2\rangle_g$ state to the $\pm|3/2\rangle_g$ state at $B_0 = 0$ T. At thermal equilibrium, we expect the relative populations of the sublevels of the ground state to be in accordance to Boltzmann's distribution,

$$\frac{N_{|\pm 3/2\rangle_g}}{N_{|\pm 1/2\rangle_g}} = \exp\left(\frac{|2D|}{k_B T_{\text{Ruby}}}\right), \quad (4)$$

where $N_{|\pm 1/2\rangle_g}$ and $N_{|\pm 3/2\rangle_g}$ are the spin populations in states $|\pm 1/2\rangle_g$ and $|\pm 3/2\rangle_g$, and T_{Ruby} is the local lattice temperature.

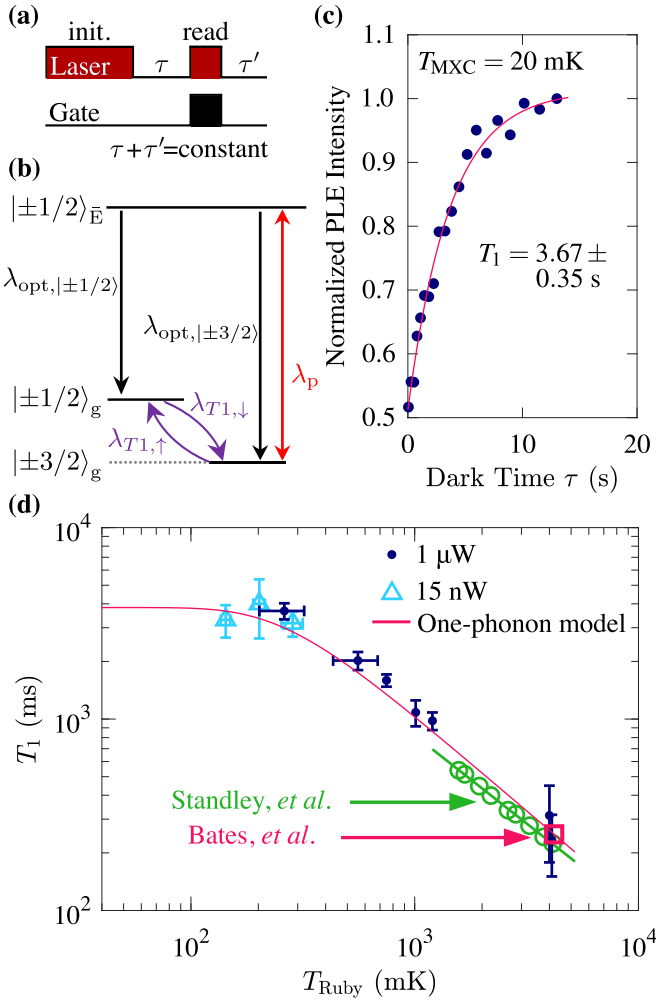


FIG. 3. (a) Pulse sequence for the all-optical T_1 measurement. (b) Rate model and transition rates describing the electron spin dynamics of the Cr^{3+} ground and excited state. See Appendix B for more details. (c) T_1 spin decay curve measured at $T_{\text{MXC}} = 20$ mK (base), $B_0 = 0$ T, and $1 \mu\text{W}$ laser excitation power. (d) Temperature dependence of T_1 as a function of lattice temperature T_{Ruby} . The solid circles correspond to data measured with $1 \mu\text{W}$ laser power, and the open triangles are confirmation measurements with 15 nW laser power for low temperatures. The open circles and the open square are literature values from Standley *et al.* [9] and Bates *et al.* [20], respectively, shown for comparison. The literature value from Bates *et al.* [20] is additionally used to infer the T_1 at lower temperature assuming the one-phonon process described by Eq. (7) (solid line).

The measurement of T_1 requires a deviation from the thermal equilibrium (initialization). This is achieved by optically pumping the $|\pm 3/2\rangle_g \leftrightarrow \bar{E}$ transition to deplete $|\pm 3/2\rangle_g$ of electrons and cycle them into $|\pm 1/2\rangle_g$. We optically pump the system until a steady-state population has been reached. At $1 \mu\text{W}$ of laser power, we measure the initialization time constant to be 0.65 ± 0.13 s [see Figs. 5(a) and 5(b) in Appendix A]. Hence, by ~ 3 s we achieve steady state, and based on the PL intensities, we transfer $\sim 45\%$ of the thermal $|\pm 3/2\rangle_g$ population to $|\pm 1/2\rangle_g$.

The initialization pulse is the first pulse in the T_1 measurement sequence shown in Fig. 3(a). This is followed by a dark

time τ of variable length in which the spins relax. A second laser pulse in resonance with the $|\pm 3/2\rangle_g \leftrightarrow \bar{E}$ transition is used to read out the ground-state spin population $N_{|\pm 3/2\rangle_g}$. We determine that the readout pulse length needs to be ≤ 0.1 s in order to ensure $N_{|\pm 3/2\rangle_g}$ to be proportional to the total PL counts, which is achieved by measuring the spin signal as a function of optical pumping time in Fig. 6(b) in Appendix C, and verifying this with rate simulations based on the model shown in Fig. 3(b). The optical decay rate from the \bar{E} excited state to the 4A_2 ground state $\lambda_{\text{opt}} = \lambda_{\text{opt},|\pm 1/2\rangle} + \lambda_{\text{opt},|\pm 3/2\rangle}$ is determined by measuring the optical decay time $T_{1,\text{opt}} = 3.6 \pm 0.2$ ms [see Fig. 5(e)]. The spin relaxation rates $\lambda_{T_1,\downarrow}$ and $\lambda_{T_1,\uparrow}$ have the following two relationships,

$$\lambda_{T_1,\downarrow} + \lambda_{T_1,\uparrow} = T_1^{-1}, \quad (5)$$

$$\frac{\lambda_{T_1,\downarrow}}{\lambda_{T_1,\uparrow}} = \exp\left(\frac{|2D|}{k_B T_{\text{Ruby}}}\right). \quad (6)$$

The pump rate λ_p into the excited state is laser power dependent when resonantly driving the $\pm 3/2\rangle_g \leftrightarrow \bar{E}$ transition, and can be determined based on optical pumping decay curves.

It is sufficient to only collect the PL emitted over the readout period, hence we set the “gate” channel of our SPAD to only enable counting during the readout period [see Fig. 3(a)]. A final consideration for performing the T_1 measurement is to ensure that the duty cycle of the laser, and therefore the average laser power, remains equal across all measurements in order to keep the sample at constant temperature. This is achieved by adding an additional dark time τ' , as shown in Fig. 3(a), such that $\tau + \tau'$ is constant. At the base temperature of the dilution refrigerator ($T_{\text{MXC}} = 20$ mK), we measure $T_1 = 3.67 \pm 0.35$ s as shown in Fig. 3(c).

Figure 3(d) shows the measured T_1 at varying lattice temperatures T_{Ruby} . The T_{Ruby} of the measurements at 15 nW laser power (light blue triangles) were determined in Sec. V. Further T_1 measurements were performed with $1 \mu\text{W}$ laser power (dark blue circles), and the corresponding T_{Ruby} were determined using similar methods to Sec. V, where at $T_{\text{MXC}} = 20$ mK and $T_{\text{MXC}} = 500$ mK, we calculate $T_{\text{Ruby}} = 262 \pm 59$ mK and $T_{\text{Ruby}} = 560 \pm 130$ mK, respectively. For $T_{\text{MXC}} > 500$ mK, we assume that $T_{\text{MXC}} \approx T_{\text{Ruby}}$. Assuming that the T_1 relaxation is dominated by a one-phonon (direct) process, we expect the following well-known relationship,

$$T_1^{-1} = A \coth\left(\frac{|2D|}{2k_B T_{\text{Ruby}}}\right), \quad (7)$$

where A is the coefficient of spontaneous emission rate [30]. Previous experimental results have shown that T_1 is dominated by the one-phonon process for Cr^{3+} concentrations $< 0.01\%$ at low temperatures [10]. At higher concentrations, cross-relaxation and exchange interaction between pairs of Cr^{3+} ions may deviate the temperature dependence of T_1 from the one-phonon process. Figure 3(d) also shows T_1 as a function of temperature in a study by Standley *et al.* [9] (open circles) supporting the one-phonon process relationship > 1.6 K, shown for comparison. The discrepancy with our measured values arises from the fact that Ref. [9]’s data were measured with $B_0 = 330$ mT parallel to the crystal axis, across the pure $|\pm 1/2\rangle$ ground-state transition, and at a

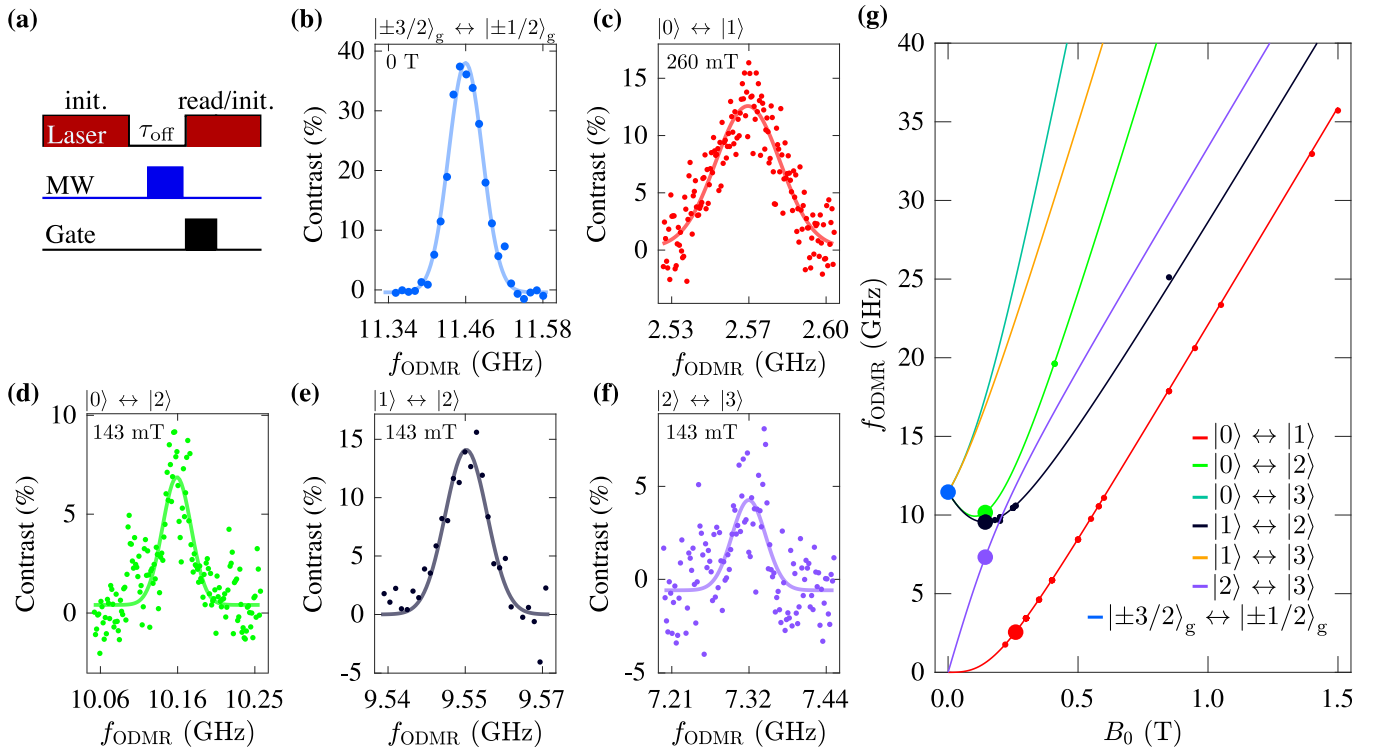


FIG. 4. (a) Pulse sequence for implementing pulsed ODMR. The initialization laser pulse is 3 s long, and the second laser pulse is also 3 s long and acts as a readout and reinitialization pulse. Within the $\tau_{\text{off}} = 10$ ms dark time, a MW pulse of $10 \mu\text{s}$ –1 ms length is applied, aligned to occur just before the readout pulse. The SPAD is gated to detect photons for the first 0.1 s of readout. The laser excitation power is 1–10 μW . (b)–(f) ODMR transitions with linewidths [full width at half maximum (FWHM)] (b) 62.0 ± 4.3 MHz, (c) 38.2 ± 4.7 MHz, (d) 32.7 ± 4.9 MHz, (e) 8.8 ± 2.0 MHz, and (f) 52 ± 17 MHz. (g) All ODMR transition frequencies measured, superimposed with expected transition frequencies given by Eq. (1). The data points obtained from (b)–(f) are emphasized with larger circles.

concentration of 0.017%, different from our experimental condition. To conform to our conditions, we consider the study by Bates *et al.* [20], which has shown that at $B_0 = 0$ T and 4.2 K, the spin relaxation is limited to $T_1 = 250 \pm 20$ ms for Cr^{3+} concentrations $< 0.02\%$ (open square). This result provides us with the spontaneous emission rate $A = 0.252 \text{ s}^{-1}$ for Eq. (7), and as our sample concentration of 0.005% falls well below the mentioned thresholds, the temperature dependence of T_1 can be completely predicted below 4.2 K by the one-phonon model [Eq. (7)], and is shown in Fig. 3(d) as a solid line. Our measured T_1 is in excellent correspondence.

Early results have found that the spin relaxation at low temperatures can ultimately depend on a number of parameters, such as growth method, chromium concentration, measurement frequency, chemical purity, and magnetic field strength and angle [9,31].

VII. OPTICALLY DETECTED MAGNETIC RESONANCE

In this section we perform optically detected electron spin resonance in between the spin states of the 4A_2 ground state. The pulse sequence to implement ODMR is shown in Fig. 4(a). We set our Ti:sapphire laser in resonance with a particular spin state $|i\rangle$ and the optically excited $|\pm 1/2\rangle_E$ state. By applying a laser pulse at this wavelength, we deplete the electron population in $|i\rangle$ via optical cycling into other states, just as we did with the laser initialization pulse in Sec. VI. In the dark time τ_{off} after the laser pulse, a MW pulse is

delivered to the sample via the PCB antenna mounted above the ruby sample. As discussed in Sec. III, the antenna creates an oscillating magnetic field $B_1 \parallel B_0$. If the MW pulse is resonant with a transition between $|i\rangle$ and any other spin level $|j\rangle$, we satisfy the resonance condition and reintroduce some population into $|i\rangle$. Finally, we use a readout laser pulse, as in Sec. VI, to measure the population in $|i\rangle$ at the end of the MW pulse.

We perform this measurement across various transitions, for magnetic fields $0 \leq B_0 \leq 1.5$ T and transition frequencies up to 36 GHz, with some examples shown in Figs. 4(b)–4(f). The ODMR contrast measured is the percentage change in the $|i\rangle$ population due to a resonant MW pulse, compared to the initialized population. The positive contrast values in all scans indicate that our initialization pulse is depleting the state $|i\rangle$ to a population that is always less than the population of $|j\rangle$.

In Appendix D we provide time evolution simulations of the magnetically driven transitions $|0\rangle \leftrightarrow |1\rangle$, $|0\rangle \leftrightarrow |2\rangle$, and $|1\rangle \leftrightarrow |2\rangle$ under the condition $B_0 \perp c$ axis, as in our experiments. The simulations show that with the B_1 direction perfectly aligned with either the c axis or B_0 , some transitions are theoretically forbidden, and not all transitions in Figs. 4(b)–4(f) should be observable with our experimental setup (see also Ref. [12]). We conclude therefore that our B_1 field must also have a small component along the c axis.

In Fig. 4(g) we mark all observed transitions frequencies onto the theoretical transition frequencies from Eq. (1), in good correspondence [data points from Figs. 4(b)–4(f)]

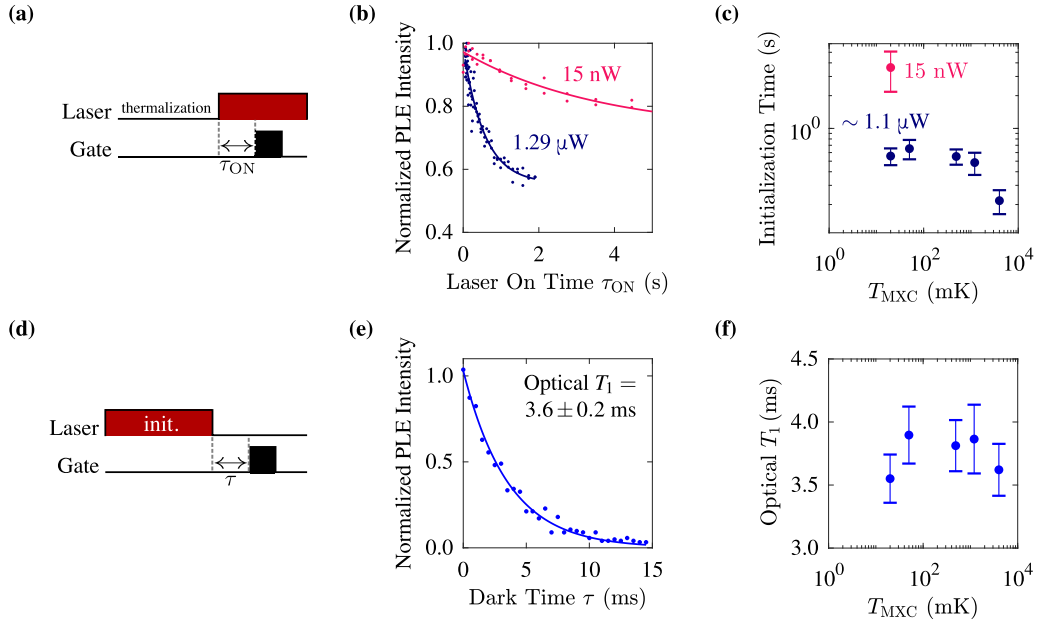


FIG. 5. (a) Pulse sequence for measuring the initialization time constant. (b) PL signal as a function of laser on-time τ_{ON} before detecting photons at $T_{MXC} = 20$ mK. (c) Extracted initialization time constants as a function of temperature T_{MXC} . (d) Pulse sequence for measuring the optical relaxation time $T_{1,opt}$. (e) Optical relaxation time $T_{1,opt}$ measurement at $T_{MXC} = 20$ mK. (f) $T_{1,opt}$ dependence on temperature T_{MXC} .

are marked as larger circles]. Noticeable here is that the ground-state Hamiltonian hosts two clock transitions: $|0\rangle \leftrightarrow |2\rangle$ at $B_0 = 103$ mT and $|1\rangle \leftrightarrow |2\rangle$ at $B_0 = 143$ mT. The latter one was observed [see Fig. 4(e)] and exhibits the minimum linewidth of 8.8 ± 2.0 MHz of all transitions measured. Finally, it is worth noting that the broadening of the zero-field ODMR shown in Fig. 4(b) is predominantly due to the dispersion of the zero-field splitting parameter D in Eq. (1), due to variations in local strain near Cr^{3+} ions [32].

VIII. CONCLUSION

In this paper, we perform a spin characterization of Cr^{3+} ions in Al_2O_3 (ruby) at ultralow temperatures $T \ll 1$ K. We optically read out the $S = 3/2$ spin state populations using photoluminescence excitation spectroscopy with phonon sideband detection. We conduct thermometry by measuring the relative populations as a function of magnetic field, and demonstrate that a lattice temperature as low as $T_{\text{Ruby}} = 143 \pm 7$ mK can be achieved under continuous laser excitation. This allows us to perform spin relaxation measurements in the temperature range $T \ll 1$ K. We measure a maximum spin relaxation time of $T_1 = 3.67 \pm 0.35$ s and confirm that the spin relaxation dynamics are governed by a direct, one-phonon process for ultralow temperatures. Furthermore, we perform optically detected magnetic resonance in between the 4A_2 ground-state spin levels, observing transitions up to 36 GHz.

ACKNOWLEDGMENTS

We acknowledge support from the Australian Research Council (Grant No. LE160100069). A.L. acknowledges sup-

port through the UNSW Scientia Program. T.S. acknowledges support from the TUM Graduate School.

APPENDIX A: DETERMINING PUMP INITIALIZATION TIME AND OPTICAL T_1

The measurement of the spin relaxation time T_1 (see Sec. VI) and ODMR (see Sec. VII) requires an initialization laser pulse to polarize the ground-state spins away from their thermal (Boltzmann) equilibrium. This initialization pulse must be long enough to reach a steady state in population, allowing us to start with the same initial ground-state population for every repetition of the measurement sequences shown in Figs. 3(a) and 4(a). Figure 5(a) depicts the pulse sequence that we use to determine this initialization time. After a long (20 s $\gg T_1$) dark time to allow the spin populations to return to their thermal equilibrium, we turn on the laser and monitor the PL as a function of on-time τ_{ON} by shifting the gating pulse for the SPAD to later times. In Fig. 5(b) we plot the reduction in PL intensity as a function of laser on-time. The graphs demonstrate how quickly and efficiently the laser depopulates the state in resonance for 15 nW (red points) and 1.3 μ W (blue points) laser power. The solid lines are exponential fits to the data indicating an initialization time constant of 3.6 ± 1.4 s for 15 nW and 0.55 ± 0.10 s for 1.3 μ W laser power, based on which we set the initialization pulse time to be 10 and 3 s, respectively. We also plot the temperature dependence of the initialization time constant in Fig. 5(c). At low temperatures it stays fairly constant and then starts reducing for $T_{MXC} > 0.5$ K. This is due to the fact that the initialization time is determined by both the pump rate λ_p as defined in Fig. 3(b), as well as the spin relaxation rate T_1^{-1} . For λ_p approaching 0 Hz, the initialization rate will approach T_1^{-1} . For λ_p being comparable to T_1^{-1} , which we show to be

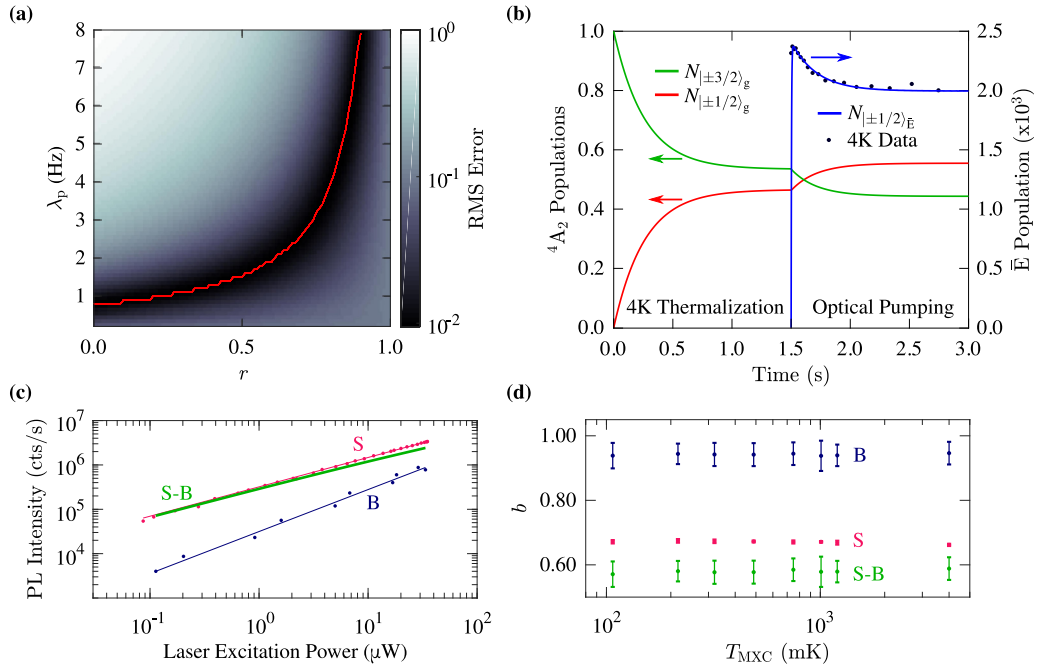


FIG. 6. (a) Root-mean-square errors of best fits to the 1- μ W, 4-K spin initialization curve as a function of laser pump rate λ_p and branching ratio r . The red line indicates the curve of the lowest fitting error. (b) Simulation of the spin initialization measurement using the rate model Eq. (B1), with $\lambda_p = 1.5$ Hz and $r = 0.5$. The populations $N_{|\pm 1/2\rangle_g}$ (red line), $N_{|\pm 3/2\rangle_g}$ (green line), and $N_{|\pm 1/2\rangle_E}$ (blue line) are superimposed with the experimental data in arbitrary units (black circles). (c) Excitation power dependence at $T_{\text{MXC}} = 20$ mK of the PLE signal “S” (red circles), and the background “B” (blue circles) with fits in the form ax^b , where x is the laser excitation power. The green line shows the expected signal with the background subtracted “S-B.” (d) Extracted exponential b from the excitation power dependence in (c) performed at varying T_{MXC} .

true in Appendix B, a change in T_1 will have an observable effect on the overall initialization time.

The pulse sequence for measuring the optical relaxation time $T_{1,\text{opt}}$ is depicted in Fig. 5(d). $T_{1,\text{opt}}$ is found by optically pumping the system with a laser pulse, then turning it off, and monitoring the PL as a function of wait time τ . This is again realized by shifting the gating pulse for the SPAD to later times. We plot the PL decay curve in Fig. 5(e), where the solid line is an exponential fit to the data. We find $T_{1,\text{opt}} = 3.55 \pm 0.19$ ms in this measurement, with no observable dependence on temperature [see Fig. 5(f)]. The optical $T_{1,\text{opt}}$ in ruby is well known in literature, going back to the first measurements by Becquerel with his phosphoroscope in 1867 [1]. It stays relatively constant for temperatures

below 300 K [33,34], and is in good agreement with our data.

APPENDIX B: RATE MODEL

We refer to the rate model and transition rates depicted in Fig. 3(b) of Sec. VI, which are applicable for $B_0 = 0$ T only. For all experiments performed in Secs. VI and VII at $B_0 = 0$ T, only the transition $|\pm 3/2\rangle_g \leftrightarrow |\pm 1/2\rangle_E$ has been resonantly excited with a laser. Hence, the rate model only includes a single pump rate λ_p (units of Hz) across this transition. The time evolution of the model is simulated in MATLAB using Runge-Kutte methods, using the following rate equations:

$$\begin{pmatrix} \dot{N}_{|\pm 1/2\rangle_E} \\ \dot{N}_{|\pm 1/2\rangle_g} \\ \dot{N}_{|\pm 3/2\rangle_g} \end{pmatrix} = \begin{pmatrix} -(\lambda_p + \lambda_{\text{opt},|\pm 1/2\rangle} + \lambda_{\text{opt},|\pm 3/2\rangle}) & 0 & 0 \\ \lambda_{\text{opt},|\pm 1/2\rangle} & \lambda_p & 0 \\ \lambda_p + \lambda_{\text{opt},|\pm 3/2\rangle} & \lambda_{T_1,\downarrow} & -(\lambda_p + \lambda_{T_1,\uparrow}) \end{pmatrix} \begin{pmatrix} N_{|\pm 1/2\rangle_E} \\ N_{|\pm 1/2\rangle_g} \\ N_{|\pm 3/2\rangle_g} \end{pmatrix}. \quad (\text{B1})$$

$N_{|i\rangle}$ is the electron population of the level $|i\rangle$, $\dot{N}_{|i\rangle} = \frac{dN_{|i\rangle}}{dt}$, and $(N_{|\pm 1/2\rangle_E} + N_{|\pm 1/2\rangle_g} + N_{|\pm 3/2\rangle_g}) = 1$. The individual spontaneous emission rates $\lambda_{\text{opt},|\pm 1/2\rangle}$ and $\lambda_{\text{opt},|\pm 3/2\rangle}$ are not determined in this study, however, we set $T_{1,\text{opt}} = \lambda_{\text{opt},|\pm 1/2\rangle} + \lambda_{\text{opt},|\pm 3/2\rangle} = (3.6 \text{ ms})^{-1}$ ms. The ground-state spin T_1 parameters can be calculated based on Eqs. (5) and (6). Without the knowledge of the T_1 parameters determined in this paper, we can perform a simulation at 4 K based on the literature value

of $T_1 = 0.26$ ms at $B_0 = 0$ T, as in Ref. [20]. Based only on the simple model in Fig. 3(b), the unknown variables are then the pump rate λ_p and the branching ratio

$$r = \frac{\lambda_{\text{opt},|\pm 3/2\rangle}}{(\lambda_{\text{opt},|\pm 3/2\rangle} + \lambda_{\text{opt},|\pm 1/2\rangle})}, \quad (\text{B2})$$

which is the probability of spontaneous emission into the $|\pm 3/2\rangle_g$ state.

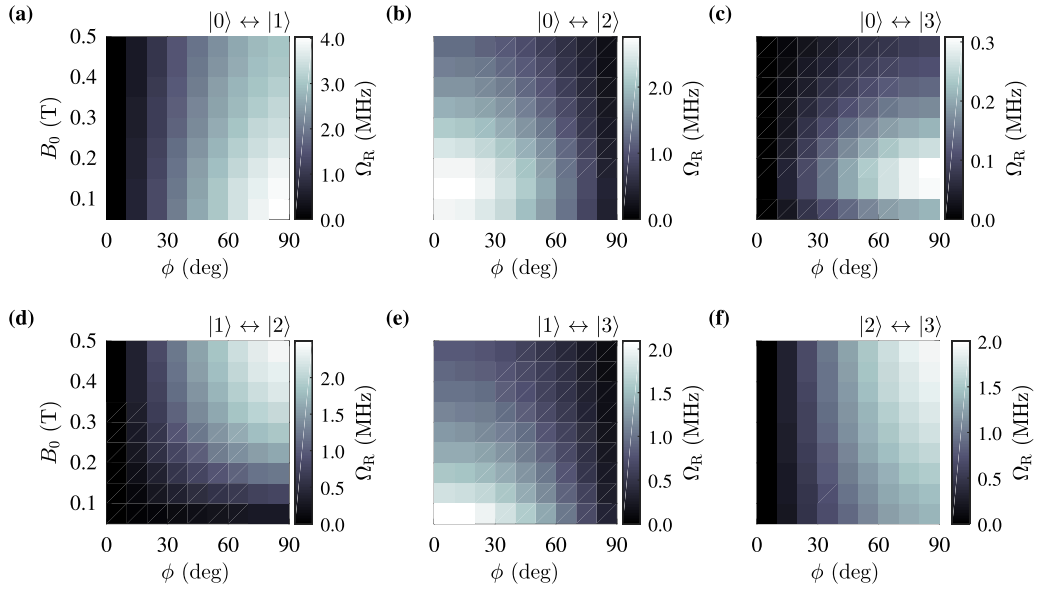


FIG. 7. (a)–(f) Rabi frequencies Ω_R extracted from time evolution simulations for transitions (a) $|0\rangle \leftrightarrow |1\rangle$, (b) $|0\rangle \leftrightarrow |2\rangle$, (c) $|0\rangle \leftrightarrow |3\rangle$, (d) $|1\rangle \leftrightarrow |2\rangle$, (e) $|1\rangle \leftrightarrow |3\rangle$, and (f) $|2\rangle \leftrightarrow |3\rangle$ as a function of B_0 strength and B_1 direction as specified by ϕ .

We first simulate the spin initialization time measurement [see the pulse sequence in Fig. 5(a)]. We sweep the parameters r and λ_p , and for each pair of values we perform a best fit to the experimental spin initialization decay curve at 4 K and 1 μ W of laser excitation power. Figure 6(a) shows the root-mean-square error of the performed fits. A range of values can adequately fit the 4 K initialization decay curve (red line), illustrating that there is no unique pair of values. Early results have determined that $r \approx 0.55$ [24,26], hence based on the solutions shown in Fig. 6(a), we expect the pump rate $\lambda_p \approx 1.7$ Hz at $T_{\text{MXC}} = 4$ K and 1 μ W laser power.

Figure 6(b) depicts the output of the simulation for the case of $\lambda_p = 1.5$ Hz and $r = 0.5$ [any pair of values on the red curve in Fig. 6(a) would result in a similar simulation output]. Assuming we begin with zero electron occupancy in the $|\pm 1/2\rangle_g$ state (red line) and complete electron occupancy in the $|\pm 3/2\rangle_g$ state (green line) with the laser off ($\lambda_p = 0$ Hz), the ground-state populations converge to thermal equilibrium in accordance with their Boltzmann factors at 4 K at the rate of $1/T_1$. At 1.5 s into the simulation, we set $\lambda_p > 0$ Hz and track the population in all three states. At the end of 3 s, the ground-state populations converge to a new steady-state distribution. At all times, $N_{|\pm 1/2\rangle_g}$ is assumed to be proportional to the optical emission. For the values chosen, the simulation is in good agreement with the measured data at 4 K (black circles).

APPENDIX C: EFFECT OF SPIN PUMPING ON MEASUREMENTS

In addition to the PLE signal being proportional to $N_{|\pm 1/2\rangle_g}$, it is also proportional to $N_{|\pm 3/2\rangle_g}$ at any point in time the laser is pumping the $|\pm 3/2\rangle_g \leftrightarrow |\pm 1/2\rangle_g$ transition. For the solutions obtained in Fig. 6(b), we confirm that regardless of the gate pulse duration chosen, the integrated PL will have some linear relationship to the population in $|\pm 3/2\rangle_g$ prior to the gate pulse (Pearson- $r > 0.99$). This is sufficient to observe the spin T_1 decay in Fig. 3. However, in the case of short

gate pulses, the PL observed is more directly proportional (i.e., linear with no offset, where the offset represents PL that is independent of the $|\pm 3/2\rangle_g$ population prior to the gate pulse), while longer gate pulses contain increasingly large offsets. This can be clearly seen in Fig. 6(b), where the initial (thermal) spin population is quickly dissipated by the optical cycling. We choose to reduce the contribution of the spin-signal-independent contribution and maximize the proportion of the spin-signal-dependent contribution, by only collecting PL from the beginning of the readout pulse. We therefore choose a gate pulse time of 0.1 s for measurements performed at 1 μ W, and following a similar analysis, 0.5 s for measurements at 15 nW.

In Fig. 6(c), we plot the power dependence of the PLE intensity as a function of laser excitation power on a double-logarithmic scale for $T_{\text{MXC}} = 4$ K and $B_0 = 0$ T. The green curve (“S”) shows the total collected signal when the laser is in resonance with the $|\pm 3/2\rangle_g \leftrightarrow |\pm 1/2\rangle_g$ transition. The blue curve (“B”) corresponds to the background signal collected when the laser is not in resonance with any of the discrete Cr^{3+} transitions. We fit both S and B to power-law dependencies and extract their exponents. For B, we obtain an exponent of 0.95 ± 0.04 , indicating a linear power dependence. For S, the signal saturates at high excitation powers, resulting in a sublinear dependence with an exponent of 0.59 ± 0.04 . Based on the fits, we also plot the background-adjusted signal “S-B” (green curve).

In Fig. 6(d) we plot the extracted exponents as a function of temperature T_{MXC} . Notably, the exponent of the background is temperature independent and linear in power, giving us validation for removing the background from all data before analysis.

APPENDIX D: SIMULATIONS OF RABI OSCILLATIONS

In order to examine the efficiency at which we can perform magnetic resonance on various transitions, we perform

numerical simulations in MATLAB. We take the ground-state Hamiltonian \mathcal{H}_0 [Eq. (1)], and apply $B_0 \perp c$ axis, along the x axis without loss of generality. We add a time-dependent part \mathcal{H}_1 that describes the effect of a linearly polarized microwave field with strength $B_1 = 100 \mu\text{T}$,

$$\mathcal{H}_1 = [g_{\parallel} \sin(\phi)S_z + g_{\perp} \cos(\phi)S_x]\mu_B B_1 \sin(\omega t), \quad (\text{D1})$$

where ω is the angular frequency of the driving field and ϕ is the angle between B_1 and B_0 . Here, $\phi = 0^\circ$ corresponds to $B_1 \parallel B_0$ along the x axis, and $\phi = 90^\circ$ corresponds to $B_1 \parallel c$ axis along the z axis. The case of B_1 along the y axis, i.e., $B_1 \perp c$ axis while also $B_1 \perp B_0$, is not considered.

In Fig. 7 we plot the extracted Rabi frequencies as a function of B_0 magnitude (for $0.05 \text{ T} \leq B_0 \leq 0.5 \text{ T}$), and B_1 direction as specified by ϕ (for $0^\circ \leq \phi \leq 90^\circ$). The result for the transition $|0\rangle \leftrightarrow |1\rangle$ is shown in Fig. 7(a), for $|0\rangle \leftrightarrow |2\rangle$ in Fig. 7(b), for $|0\rangle \leftrightarrow |3\rangle$ in Fig. 7(c), for $|1\rangle \leftrightarrow |2\rangle$ in Fig. 7(d), for $|1\rangle \leftrightarrow |3\rangle$ in Fig. 7(e), and for $|2\rangle \leftrightarrow |3\rangle$ in Fig. 7(f). At

$B_0 = 0 \text{ T}$ (not shown), irrespective of ϕ , only the $|0\rangle \leftrightarrow |2\rangle$ and $|1\rangle \leftrightarrow |3\rangle$ transitions are allowed as there would be no off-diagonal entries in Eq. (1) and as these transitions result in a spin change of 1. Based on the simulation results shown, for $B_0 > 0 \text{ T}$ and $\phi = 0^\circ$, the $|0\rangle \leftrightarrow |2\rangle$ and $|1\rangle \leftrightarrow |3\rangle$ transitions are allowed, albeit with decreasing Rabi frequency as the increasing B_0 tilts the quantization axis of \mathcal{H}_0 away from $\perp B_1$ and towards $\parallel B_1$. Under the same conditions, all other transitions are forbidden. In contrast, the case of $\phi = 90^\circ$ yields a forbidden transition for the $|0\rangle \leftrightarrow |2\rangle$ and $|1\rangle \leftrightarrow |3\rangle$ case, and allowed transitions for all other cases. See also Ref. [12] for more details.

In the main text [Figs. 4(b)–4(d)], the transitions $|0\rangle \leftrightarrow |1\rangle$, $|0\rangle \leftrightarrow |2\rangle$, $|1\rangle \leftrightarrow |2\rangle$, and $|2\rangle \leftrightarrow |3\rangle$ are observed, which is possible for intermediate values of ϕ . In other words, in order to observe all ODMR transitions with $B_0 \perp c$ axis, it suffices to have the B_1 vector parallel to the plane defined by the B_0 vector and c axis, but not aligned exactly to either.

-
- [1] E. Becquerel, *La Lumière, Ses Causes et Ses Effets: Sources de lumière* (Firmin Didot Frères, Librairie de Firmin Didot Freres, Fils et Cie, Paris, 1867), Vol. 1, pp. 337–348.
- [2] G. Imbusch and W. Yen, *Lasers, Spectroscopy and New Ideas* (Springer, Berlin, 1987), pp. 248–267.
- [3] T. H. Maiman, *Nature (London)* **187**, 493 (1960).
- [4] G. Makhov, C. Kikuchi, J. Lambe, and R. W. Terhune, *Phys. Rev.* **109**, 1399 (1958).
- [5] W. G. Farr, D. L. Creedon, M. Goryachev, K. Benmessai, and M. E. Tobar, *Phys. Rev. B* **88**, 224426 (2013).
- [6] W. G. Farr, M. Goryachev, D. L. Creedon, and M. E. Tobar, *Phys. Rev. B* **90**, 054409 (2014).
- [7] Y. Wiemann, J. Simmendinger, C. Clauss, L. Bogani, D. Bothner, D. Koelle, R. Kleiner, M. Dressel, and M. Scheffler, *Appl. Phys. Lett.* **106**, 193505 (2015).
- [8] B. Miksch, M. Dressel, and M. Scheffler, *Rev. Sci. Instrum.* **91**, 025106 (2020).
- [9] K. J. Standley and R. A. Vaughan, *Phys. Rev.* **139**, A1275 (1965).
- [10] P. L. Donoho, *Phys. Rev.* **133**, A1080 (1964).
- [11] A. A. Manenkov and A. M. Prokhorov, *Sov. Phys. JETP* **1**, 610 (1955).
- [12] E. S.-D. Bois, *Bell Syst. Tech. J.* **38**, 271 (1959).
- [13] A. A. Manenkov and V. B. Federov, *Sov. Phys. JETP* **11**, 751 (1960).
- [14] J. G. Hartnett, M. E. Tobar, J.-M. Le Floch, J. Krupka, and P.-Y. Bourgeois, *Phys. Rev. B* **75**, 024415 (2007).
- [15] S. Geschwind, R. Collins, and A. Schawlow, *Phys. Rev. Lett.* **3**, 545 (1959).
- [16] S. Geschwind, G. Devlin, R. Cohen, and S. Chinn, *Phys. Rev.* **137**, A1087 (1965).
- [17] G. Imbusch and S. Geschwind, *Phys. Rev. Lett.* **17**, 238 (1966).
- [18] W. F. Koehl, B. Diler, S. J. Whiteley, A. Bourassa, N. T. Son, E. Janzén, and D. D. Awschalom, *Phys. Rev. B* **95**, 035207 (2017).
- [19] R. C. Powell, *The Interaction of Chromium Ions in Ruby Crystals*, Physical Sciences Research Papers (Air Force Cambridge Research Laboratories, United States Air Force, 1966).
- [20] C. A. Bates, J. P. Bentley, R. A. Lees, and W. S. Moore, *J. Phys. C: Solid State Phys.* **2**, 1970 (1969).
- [21] G. F. Imbusch, W. M. Yen, A. L. Schawlow, G. E. Devlin, and J. P. Remeika, *Phys. Rev.* **136**, A481 (1964).
- [22] T.-T. Chang, D. Foster, and A. H. Kahn, *J. Res. Natl. Bur. Stand. (U.S.)* **83**, 133 (1978).
- [23] T. Muramoto, Y. Fukuda, and T. Hashi, *J. Phys. Soc. Jpn.* **26**, 1551 (1969).
- [24] S. Sugano and I. Tsujikawa, *J. Phys. Soc. Jpn.* **13**, 899 (1958).
- [25] H. Hori, H. Mollmotto, and M. Date, *J. Phys. Soc. Jpn.* **46**, 908 (1979).
- [26] D. F. Nelson and M. D. Sturge, *Phys. Rev.* **137**, A1117 (1965).
- [27] V. K. Sewani, H. H. Vallabhapurapu, Y. Yang, H. R. Firgau, C. Adambukulam, B. C. Johnson, J. J. Pla, and A. Laucht, *Amer. J. Phys.* (to be published), [arXiv:2004.02643](https://arxiv.org/abs/2004.02643).
- [28] R. Terhune, J. Lambe, C. Kikuchi, and J. Baker, *Phys. Rev.* **123**, 1265 (1961).
- [29] F. Haupt, A. Imamoglu, and M. Kroner, *Phys. Rev. Applied* **2**, 024001 (2014).
- [30] L. T. A. Ho and L. F. Chibotaru, *Phys. Rev. B* **97**, 024427 (2018).
- [31] D. R. Mason and J. S. Thorp, *Phys. Rev.* **157**, 191 (1967).
- [32] C. J. Kirkby and J. S. Thorp, *J. Phys. C: Solid State Phys.* **1**, 913 (1968).
- [33] Z. Zhang, K. T. V. Grattan, and A. W. Palmer, *Phys. Rev. B* **48**, 7772 (1993).
- [34] D. Chandler, Z. Majumdar, G. Heiss, and R. Clegg, *J. Fluoresc.* **16**, 793 (2006).